

Temporal Properties of Cygnus X–1 During the Spectral Transitions

Wei Cui¹, S. N. Zhang², W. Focke³⁴, and J. H. Swank³

ABSTRACT

We report the results from our timing analysis of 15 *Rossi X-ray Timing Explorer* (RXTE) observations of Cygnus X–1 throughout its 1996 spectral transitions. The entire period can be divided into 3 distinct phases: (1) transition from the hard state to the soft state, (2) soft state, and (3) transition from the soft state back to the hard state. The observed X-ray properties (both temporal and spectral) in Phases 1 and 3 are remarkably similar, suggesting that the same physical processes are likely involved in triggering such transitions. The power density spectrum (PDS) during the transition can be characterized by a low-frequency red noise (power law) component, followed by a white noise (flat) component which extends to roughly 1–3 Hz where it is cut off, and a steeper power law ($\sim 1/f^2$) at higher frequencies. The X-ray flux also exhibits apparent quasi-periodic oscillation (QPO) with the centroid frequency varying in the range of 4–12 Hz. The QPO shows no correlation with the source flux, but becomes more prominent at higher energies. This type of PDS bears resemblance to that of other black hole candidates often observed in a so-called very high state, although the origin of the observed QPO may be very different. The low-frequency red noise has not been observed in the hard state, thus seems to be positively correlated with the disk mass accretion rate which is presumably low in the hard state and high in the soft state; in fact, it completely dominates the PDS in the soft state. In the framework of thermal Comptonization models, Cui et al. (1997a) speculated that the difference in the observed spectral and timing properties between the hard and soft states is due to the presence of a “fluctuating” Comptonizing corona during the transition. Here we present the measured hard X-ray time lags and coherence functions between various energy bands, and show that the results strongly support such scenario.

Subject headings: binaries: general — stars: individual (Cygnus X–1) — X-rays: stars

¹Room 37-571, Center for Space Research, Massachusetts Institute of Technology, Cambridge, MA 02139

²ES-84, NASA/Marshall Space Flight Center, Huntsville, AL 35812

³NASA/Goddard Space Flight Center, Code 662, Greenbelt, MD 20771

⁴also Department of Physics, University of Maryland, College Park, MD 20741

1. INTRODUCTION

Cygnus X–1 is one of the best studied X–ray sources. It was discovered in 1965 (Bowyer et al. 1965), and its binary nature was soon established with the detection of an orbital period of 5.6 days (Bolton 1972; Webster & Murdin 1972). The optical radial–velocity measurements indicate that the compact object has a mass in excess of $\sim 7M_{\odot}$ and a probable mass of $\sim 16M_{\odot}$ (Gies & Bolton 1982, 1986), strongly suggesting that there is a black hole in the system.

Cyg X–1 belongs to the class of high–mass X–ray binaries. Its companion was identified as a O9.7 Iab supergiant with a mass in excess of $\sim 20M_{\odot}$ and a probable mass of $\sim 33M_{\odot}$ (Gies & Bolton 1986). Stellar wind is, therefore, postulated to play an important role in producing X–rays. It is thought that the companion star is very close to filling its Roche Lobe, and the X–ray emission is driven by so–called “focused wind accretion” (Gies & Bolton 1986).

The long–term monitoring of Cyg X–1 revealed that its soft X–ray flux ($\lesssim 10$ keV) shows, on average, two distinct levels (Holt et al. 1976; Cui et al. 1997a), which are often referred to as the low and high states in the literature for historical reasons. Such terminology can often be very confusing because the hard X–ray flux ($\gtrsim 10$ keV) is anti–correlated with the soft flux during the transition — the soft X–ray low state is actually hard X–ray high (Dolan et al. 1977; Ling et al. 1987; Cui et al. 1997a). The observed X–ray properties of Cyg X–1 depend strongly on which state it is in. It is usually in the soft X–ray low state where the energy spectrum is relatively flat (or hard), and can be characterized by a single power law with a photon index of ~ 1.7 (cf. review by Tanaka & Lewin 1995). Occasionally, it reaches the soft X–ray high state where the power–law energy spectrum becomes significantly steeper (or softer; with a photon index of ~ 2.5). Therefore, “hard state” and “soft state” are more precise terms in describing the bi–modal behavior. Despite extensive investigation (observational and theoretical) for the past couple of decades, it is still not clear what triggers the spectral transitions.

The X–ray spectrum of Cyg X–1 extends beyond 100 keV in both states (e.g., Phlips et al. 1996; Cui et al. 1997a), which presents challenge to theoretical models. It is generally thought that the hard X–ray emission is the result of low–energy photons being up–scattered by hot electrons in the system (e.g., Shapiro, Lightman, & Eardley 1976; review by Narayan 1996b, and references therein). The soft photons probably originate in the synchrotron emission from relativistic electrons or the thermal emission from an accretion disk. However, little is known about the origin of Comptonizing electrons. Thermal Comptonization requires extremely high electron temperature ($\sim 10^9$ K) to reach the observed cutoff energy (Sunyaev & Titarchuk 1980; Payne 1980). The preliminary results from a recent simultaneous RXTE/OSSE observation of Cyg X–1 in the soft state show that the power–law energy spectrum extends up to ~ 600 keV without any breaks (Phlips et al. 1997). If confirmed, they would be at odds with those that require a “cooled” Comptonizing region in the soft state, and push others to the physical limits as well. Alternatively, in the soft state, the bulk motion of relativistic electrons near the black hole may be more efficient in up–scattering soft photons than the thermal motion (Titarchuk,

Mastichiadis, & Kylafis 1996). Calculations show that such bulk motion can produce the observed spectral characteristics (Chakrabarti & Titarchuk 1995; Ebisawa, Titarchuk, & Chakrabarti 1996; Titarchuk 1997).

There is, however, a tendency that the temporal properties are not emphasized enough and sometimes are completely ignored in the model. X-ray variability carries rich information about X-ray emitting regions, instabilities in the accretion disk, temporal evolution of the disk and Comptonizing region during the transition, and even the condition about the companion star (e.g., Roche Robe overflow versus focused wind accretion). Of course, high signal-to-noise and high timing resolution data are essential for such studies, especially phenomena in the vicinity of the black hole where dynamical time scales are on the order of tens or hundreds of microseconds. The RXTE data have much better simultaneous spectral and timing information than was previously available.

RXTE provides unprecedented true μ s timing resolution and covers a broad energy range (Bradt, Rothschild, & Swank 1993). The *All-Sky Monitor* (ASM; Levine et al. 1996) aboard routinely monitors known bright sources (in the 1.3–12 keV energy band). On 1996 May 10 (MJD 50213), it revealed that Cyg X-1 started a transition from the normal hard state to the soft state (Cui 1996; Cui, Focke, & Swank 1996). After reaching the soft state, it stayed for nearly 2 month before going back down to the hard state (Zhang, Harmon, & Paciesas 1996). Figure 1 shows the ASM light curve that covers the entire period.

This period can be divided into 3 distinct phases: (1) hard-to-soft transition, (2) soft state, and (3) soft-to-hard transition. The transitions are characterized by a fast rise (or decay) in the ASM flux. The soft-to-hard transition is nearly a mirror image of the hard-to-soft transition. Although the ASM flux of the source is, on average, \sim 0.4 Crab in the hard state and \sim 1.1 Crab in the soft state, it varies greatly on time scales of minutes to days in both states, with a significantly larger amplitude in the soft state.

Snapshots of Cyg X-1 were taken with the main pointing detectors on RXTE, namely, the *Proportional Counter Array* (PCA; 2–60 keV) and *High-energy X-ray Timing Experiment* (HEXTE; 15–250 keV), to monitor its temporal and spectral variability throughout the entire period. In this paper we present the results from the timing analysis of the PCA observations. Preliminary spectral and timing results, based on the observations during the hard-to-soft transition and some in the soft state, were already reported in Belloni et al. (1996) and Cui et al. (1997a, b). For comparison, however, these observations were re-analyzed in the same way as subsequent ones for the soft state and the soft-to-hard transition. Table 1 briefly summarizes some basic information on the observations, which are also marked with symbols in Figure 1.

As discussed in Cui et al. (1997a,b) the source went through a sequence of states with the soft X-ray flux (< 10 keV) and the hard flux (> 20 keV) both changing. The soft flux alone was an incomplete indicator of the states. The RXTE observations with the pointing instruments were only snapshots. Systematic study of the spectral and timing properties during these snapshots

and comparison of the BATSE and ASM behavior during the ASM soft outburst imply that the source went through a transition over a period of 20 days to a soft state which persisted for about 55 days and then made a transition back to the hard state again taking about 20 days.

2. ANALYSIS

The PCA observations were made consistently with the following set of data modes (Morgan et al. 1994): a Binned mode with 4 ms time bin and 8 energy bands in the range of 2–13.1 keV, a Event mode with 16 μ s time bin and 16 energy bands above 13.1 keV, and two Single–Bit modes with 122 μ s time bin, covering the energy bands 2–6.5 keV and 6.5–13.1 keV, respectively. The results presented here are derived from the Event–mode data and Single–Bit data. For brevity, the energy bands 2–6.5 keV, 6.5–13.1 keV, and 13.1–60 keV are referred to as the soft band, medium band, and hard band, respectively.

Since all other observations contain only one orbit worth of data, we chose to break up the first and second observation (see Table 1) into individual orbits, each of which was analyzed separately. It should be noted that the first observation actually consists of only two orbits, but one of the five detectors was turned off (for safety reasons) during the second orbit. To simplify the analysis, the second orbit was broken up into two segments.

2.1. Power Density Spectrum

We chose to bin data in 2^{-6} s time bin. For each orbit, we broke up the light curve into 64-second segments. A 2^{12} –point FFT was performed on each segment to obtain a Leahy–normalized PDS. The PDSs for all segments were then averaged to obtain the average PDS, as well as its variance. Finally, from the average PDS we subtracted the Poisson noise power corrected for instrument dead–time effects. The kind of effects of dead time caused by good events were discussed by Zhang et al. (1995). Simulations show that for the real detectors, in which several effects compete (Jahoda et al. 1996), the effective dead-time can be described by the non-paralyzable formula (Equation (44) in Zhang et al. (1995)) with the detector dead-time $t_d \simeq 10\mu$ s (W. Zhang, private communication). In our case the time bin size $t_b = 2^{-6}$ s and the formula is much simplified because $t_b \gg t_d$ and the count rate is low (the time between events is large compared to the dead time). There is some spectral dependence to the dead time and while we know the form and approximate numbers, we can expect that the numbers should be adjusted. A second effect needs to be taken into account (as described in Appendix F of the XTE NRA and in Zhang et al. (1996)), the dead time due to very large events in the detector. No transmission of events is allowed for a set amount of time. For observations #5–#12 this was set to a value of about 70μ s, and for the others it was 155μ s. It is not a significant correction for the Cyg X-1 observations.

To estimate the uncertainty in calculating Poisson noise power, we obtained the PDSs that extend up to ~ 4 kHz by using finer time bins. We searched but failed to detect any QPOs at frequencies above 30 Hz in all observations. After carefully examining the PDS shape, it became apparent that the power in the highest frequency bins was purely due to photon counting statistics. We then compared the measured high-frequency power to the calculated value, and concluded that roughly 99.5% of the Poisson noise power should have been removed by following the dead time correction procedure we described. The residual becomes significant starting at ~ 30 Hz, which determined the finest time bin size we could use without losing information from PDS.

To facilitate the comparison of the results in different energy bands and from different observations, the power density is presented as the fractional rms variability, which can be derived by dividing the Leahy-normalized PDS by the mean count rate (van der Klis 1995).

2.1.1. *Transitions*

The hard-to-soft transition was covered by the first 3 observations (a total of 7 orbits worth of data), while the soft-to-hard transition by the last three (see Table 1). In both phases, the observed PDS exhibits very similar characteristics. For the purpose of illustration, Figures 2 and 3 show the PDSs in the soft, medium, and hard band, as well as the total passing band, for Observations #3 and #15, respectively, representative of each phase. From the figures, the PDS can be characterized by a red noise component at low frequencies, followed by a white noise component that extends to 1–3 Hz, above which it is cut off. At higher frequencies, the PDS becomes power law again, with a much steeper slope (roughly -2, i.e., $1/f^2$). With respect to this model of continuum, a QPO is detected in all observations. To quantify the characteristics, we model the continuum with the following function:

$$PDS(f) = \begin{cases} C(rms_c)^2 \left(\frac{f}{f_{b1}}\right)^{-\alpha_1} & f < f_{b1} \\ C(rms_c)^2 & f_{b1} \leq f < f_{b2} \\ C(rms_c)^2 \left(\frac{f}{f_{b2}}\right)^{-\alpha_2} & f \geq f_{b2}, \end{cases} \quad (1)$$

where C is a constant chosen so that rms_c is the integrated fraction rms amplitude of the continuum in the frequency range of 0.02–32 Hz. The QPO is modeled by a Lorentzian function, i.e.,

$$PDS(f) = \frac{(rms_{qpo})^2}{\pi} \frac{G/2}{(f - f_{qpo})^2 + (G/2)^2}, \quad (2)$$

where rms_{qpo} is the integrated fractional rms amplitude of the QPO, f_{qpo} is the QPO centroid frequency, and G is the full width at half maximum (FWHM). The best-fit models are summarized in Table 2. The errors shown represent 1σ confidence level. This simple model characterizes the data reasonably well, as indicated by the reduced χ^2 of the fit.

The PDS continuum varies little on a time scale of days (the time between observations), except for the high-frequency cutoff (f_{b2}) which changes quite significantly. On a shorter time

scale (between orbits), however, f_{b2} remains quite stable. It is worth noting that the derived power-law slope of the red noise (α_1) can be somewhat uncertain because of the narrow frequency range covered in the fit. It is actually closer to -1 (i.e., $1/f$ noise) when longer baselines are used (Cui et al. 1997a, b). Also shown in Figure 2 is that the continuum is energy dependent: the white noise power decreases as the photon energy increases, while f_{b2} remains roughly constant.

The QPO moves around significantly during the transition. There are no apparent correlations between the QPO characteristics and the total count rate — see Figure 4. However, the QPO is energy dependent: it becomes more prominent at higher energies, as shown in Figures 2 and 3. To investigate any spectral dependence of the QPO, we define the following hardness ratios: soft hardness ratio (HR1) is the ratio of the total source counts in the medium band to that in the soft band, and the hard hardness ratio (HR2) the hard band to the medium band. Both hardness ratios were plotted against the QPO fraction rms amplitude in Figure 5. With limited statistics, the QPO appears to strengthen as the energy spectrum becomes harder. Moreover, the QPO centroid frequency (f_{qpo}) shows strong anti-correlation with the fractional rms amplitude (rms_{qpo}) and correlation with f_{b2} — see Figure 6, which is made from Table 2.

2.1.2. Soft State

Starting from Observation #4, subsequent 9 observations cover the soft state which is characterized by a power-law PDS (Cui, Focke, & Swank 1996; Cui et al. 1997a, b). As an example, Figure 7 shows the PDSs for Observation #6 in the energy bands defined previously. The white noise is hardly detectable in this state, so the continuum is much simplified. It was modeled by a broken power law,

$$PDS(f) = \begin{cases} C(rms_c)^2 \left(\frac{f}{f_b}\right)^{-\alpha_1} & f < f_b \\ C(rms_c)^2 \left(\frac{f}{f_b}\right)^{-\alpha_2} & f \geq f_b, \end{cases} \quad (3)$$

where C is a constant chosen so that rms_c is the integrated fraction rms amplitude of the continuum in the frequency range of 0.02–32 Hz. Examining Figure 7 more carefully, there appears to be some deviation from the power-law around 6 Hz. Such feature is so broad and can hardly be called a QPO. For simplicity, these broad “bumps” are also modeled by the Lorentzian function in Equation (2). The best-fit models are shown in Table 3. In general, adding a QPO-like feature does statistically improve the fit, but such features are weak, and are not required at all in some cases. The centroid of these bumps clusters around 6–7 Hz.

The continuum varies little in the soft state. The overall PDS is dominated by the low-frequency $1/f$ noise, more so in the high energy bands. The PDS breaks consistently at ~ 13 – 14 Hz, except for Observations #9 and #12. At higher frequencies, the PDS steepens, with the power-law slope ranging from -1.9 to -2.6, which is very similar to that during the transition.

2.2. Cross Spectral Correlation

As in the previous section, we derived the average PDS and cross spectral function (defined below) for each orbit worth of data by following the same procedure, except for a finer time bin size (2^{-10} s) adopted and 2^{16} -point FFT performed on each 64-second segment. It should be pointed out that the *unnormalized* PDS is used in the calculation.

Because of the finer time bin size, much wider frequency range is covered. However, as noted in the previous section, the error in estimating Poisson noise power becomes significant above ~ 32 Hz, so the results at high frequencies should be taken with reservation.

Assuming that $F_1(f)$ and $F_2(f)$ are the Fourier series calculated for two energy bands, #1 and #2, the cross spectral function (CSF) between them is defined as

$$C(f) = F_1^*(f)F_2(f), \quad (4)$$

where $F_1^*(f)$ is the complex conjugate of $F_1(f)$.

2.2.1. Hard X-ray Time Lag

If $R(f)$ and $I(f)$ are the real and imaginary parts of CSF, the average phase difference between the two energy bands is given by

$$\Delta\phi(f) = \tan^{-1} \left(\frac{\langle I(f) \rangle}{\langle R(f) \rangle} \right), \quad (5)$$

where angle brackets stand for ensemble averaging. Its variance was estimated by simply propagating errors, i.e.,

$$\delta\Delta\phi = 0.5 |\sin(2\Delta\phi)| \left(\left| \frac{\delta \langle R \rangle}{\langle R \rangle} \right| + \left| \frac{\delta \langle I \rangle}{\langle I \rangle} \right| \right). \quad (6)$$

The average time lag (or advance if negative) of X-rays in energy band #2 with respect to those in energy band #1 is then given by

$$\Delta t = \frac{\Delta\phi}{2\pi f}. \quad (7)$$

The soft band is used as a reference band. For each of the observations listed in Table 1, the hard X-ray time lags are computed for the medium and hard bands with respect to the soft band. As for the PDS, the measured hard X-ray time lag also shows very similar characteristics within each transition and between the transitions, but are markedly different between the transition and the soft state. To illustrate this point, the results for Observations #3, #6, and #15 (one in each phase) are summarized in Figure 8. During the transition, hard X-rays clearly lag behind soft ones. The measured time lag shows a decreasing trend toward high frequency, confirming the Ginga results (Miyamoto et al. 1988). It shows a peak at the QPO frequency — most apparent

between the soft and medium bands — showing an additional time delay associated with the phenomenon. The time lag increases with photon energy. To quantify it, we defined an “effective” time lag for each energy band by simply averaging the results in the frequency range of 1–10 Hz, where error bars are small. The results are plotted in Figure 9 for all observations. We also define an “effective” energy for each energy band,

$$E_{eff} = \frac{\int di \int ER(i, E)S(E)dE}{\int di \int R(i, E)S(E)dE}, \quad (8)$$

where $S(E)$ is the photon flux at energy E , and $R(i, E)$ is the detector response matrix that distributes photons at energy E to counts in each pulse-height channel i ; energy integrals are computed over a chosen energy band, while pulse-height channel integrals are over all channels. Using the observed photon spectra for Phase 1 (Cui et al. 1997a) and PCA response matrices, the effective energy is computed for each energy band. Roughly, they are ~ 3 keV, ~ 9 keV, and ~ 27 keV for the soft, medium, and hard bands, respectively, depending only weakly on the exact spectral shape. Therefore, the time lag scales with photon energy roughly as $\log(E_1/E_0)$ during the transitions, where E_0 and E_1 represent the effective energies for any two energy bands. In the soft state, the time lags become hardly measurable between the same energy bands, and the logarithmic scaling with photon energy also breaks down.

2.2.2. Coherence Function

The coherence function is a measure of linear correlation between the two energy bands of interest (Bendat & Piersol 1986). In the noiseless case, it is defined as

$$\gamma(f) = \frac{\langle C(f) \rangle \langle C^*(f) \rangle}{\langle PDS_1(f) \rangle \langle PDS_2(f) \rangle}, \quad (9)$$

where $PDS_1(f) = F_1^*(f)F_1(f)$ and $PDS_2(f) = F_2^*(f)F_2(f)$ are the PDSs for energy bands #1 and #2, respectively. Therefore, the coherence function takes value in the range of 0 to 1, with 0 being no correlation and 1 perfect linear correlation. In reality, noises due to photon counting statistics are always present. A detailed treatment of such cases was presented and discussed thoroughly in Vaughan & Nowak (1997).

We calculated the coherence function, as well as its variance, by following the recipe presented in Vaughan & Nowak (1997), which *only* applies to the cases of high signal power and high coherence. As shown in Figures 2, 3, 7, the signal power diminishes rapidly at high frequencies, so the coherence function was calculated only at low frequencies. Figure 10 summarizes the results for Observations #3, #6, and #15, as an example to show typical characteristics for each of the three phases. During the transition, the coherence function indicates a good linear correlation between the soft and medium bands, much less so between the soft and hard bands. Nearly perfect linear correlations are observed between all three energy bands in the soft state.

As for the time lag, we averaged the coherence function between 1 and 10 Hz for all observations, and plotted the results in Figure 11. Clearly, the coherence function jumps around between observations during the transition, but remains quite stable in the soft state.

3. DISCUSSION

The observed PDS shows apparent evolution during the spectral transition. In the hard state, the PDS of Cyg X-1 can be characterized by a white noise component that extends up to ~ 0.04 – 0.4 Hz where it breaks into roughly a single power-law (review by van der Klis 1995; Belloni et al. 1996). During the hard-to-soft transition, the white noise weakens, and the cutoff frequency moves up to 1–3 Hz. In addition, a low-frequency $1/f$ component appears (see Fig 2, also Belloni et al. 1996 and Cui et al. 1997a). As the source approaches the soft state, the $1/f$ noise strengthens until it dominates the PDS in the soft state (see Fig. 3). This evolution sequence completely reverses during the soft-to-hard transition (see Fig. 4). The absence of the $1/f$ noise in the hard state and its dominance in the soft state seems to suggest that it is positively correlated with the *disk* mass accretion rate which is lower in the hard state and higher in the soft state (cf. Zhang et al. 1997). Therefore, it likely originates in the accretion disk. It can be produced by the fluctuation in the local accretion rate as a result of small random fluctuation in the viscosity (Kazanas, Hua, & Titarchuk 1996), or by the superposition of random accretion “shots” with long lifetimes (cf. Belloni & Hasinger 1990). The remarkable repeatability of the properties of Cyg X-1 as observed in recurrences of its various states and the similarity of the observed X-ray properties during the transitions from the hard to soft and soft to hard states implies an orderly dependence of the physical processes on some parameter. What are these processes and the possibilities for the parameter?

The hard X-ray emission from Cyg X-1 in the hard state and in the transition state is probably the product of thermal Comptonization. Although the exact geometry of the Comptonizing hot corona is still unknown — many have been proposed — there is evidence that it is present only in the vicinity of the black hole for X-ray binaries (e.g., Gierliński et al. 1996). The corona could be formed due to advection-dominated accretion flows (ADAF) (e.g., Narayan & Yi 1994), or as a post-shock region in a centrifugally supported shock (e.g., Chakrabarti & Titarchuk 1995). It is still highly controversial if a shock can be formed, but the essential element is a Comptonizing region for both models. The ADAF model does provide an explanation of the different states (cf. Narayan 1996b). According to this model, the standard optically thick, geometrically thin disk (Shakura & Sunyaev 1973) is only present in the outer region, and is truncated near the black hole where an optically-thin hot “corona” is formed. The “corona” rotates at sub-Keplerian speed, and dissipates angular momentum via viscous processes, so behaves just like the thin disk. However, the gas density in the “corona” is so low that radiation becomes an inefficient cooling mechanism. Consequently, gravitational energy released in the accretion process heats up the gas, and advects with it into the black hole. It was shown that when the mass accretion rate is below

some critical value, the corona is large and the thin disk is far away from the black hole — this is the low state. As the accretion rate increases, the inner edge of the disk moves inwards and the corona shrinks, due to the increased local Compton cooling efficiency; the source is on its way to the high state. When the accretion rate exceeds the critical value, this process continues until the inner edge of the disk reaches the last stable orbit — this is the high state.

Is the ADAF model consistent with our results? The answer is yes, at least qualitatively. In previous work (Cui et al. 1997a), we speculated that the white noise perhaps originates near the black hole where dynamical time scale is short compared to the frequency range of the observed power. It is then filtered by the hot corona to produce the characteristic break (f_{b2}) on the PDS. The break frequency would then be determined by the characteristic photon escape time through the corona, i.e. by its physical size (Cui et al. 1997a; also a model in Hua & Titarchuk 1996). Therefore, the increase in the break frequency as the source approaches the soft state is consistent with the corona becoming smaller, which would also explain the softer energy spectrum in the soft state (Cui et al. 1997a). The temporal evolution of the corona during the transitions can then be illustrated by the change in the break frequency.

Such a scenario is strongly supported by the measurement of hard X-ray time lag and coherence between different energy bands. The logarithmic scaling of the observed time lag with photon energy are consistent with the predictions of the thermal Comptonization in the corona (e.g., Payne 1980; Hua & Titarchuk 1996; Kazanas, Hua, & Titarchuk 1996). The much smaller lag times of the soft state do not support scaling as the log of the photon energy, implying that the large high temperature corona is not present. The loss of coherence during the transition (see Fig. 11) can also be accounted for by a varying corona. The coherence function being near unity in the soft state rules out models invoking multiple, uncorrelated emission regions to account for X-ray variability on different time scales (cf. Vaughan & Nowak 1997).

However, the current version of the ADAF model cannot satisfactorily describe as luminous an X-ray source as Cyg X-1 in the hard state. The maximum luminosity allowed by the model is $\sim 0.05\alpha^2 L_E$ (Narayan 1996a), where α is the constant that describes viscosity in the standard thin-disk model (Shakura & Sunyaev 1973), and L_E is the Eddington luminosity. For a Cyg X-1 black hole of about $10M_\odot$, the measured luminosity is about $0.03L_E$ (Zhang et al. 1997), which would require α to be on the order of unity. Thus the reason for the hard state configuration is uncertain, but the spectral and temporal properties are qualitatively in accord with several models, to the degree they are specified.

Alternatively, a shock could be formed close to the black hole in Cyg X-1. Here, the post-shock region provides Comptonizing hot electrons, so there is essentially no difference between the two models for the hard state. In the soft state, however, Chakrabarti & Titarchuk (1995) predicts the formation of a relativistic electron flow rushing towards the black hole, due to much more efficient Compton cooling. The bulk motion of the flow up-scatters soft photons to produce the observed hard X-ray emission.

With a varying corona, it is natural to ask if the detected QPO during the transition is of coronal origin. As discussed in Section 2.1.1, there is strong evidence that the observed QPO characteristics are related to hard X-ray or coronal properties: the QPO amplitude increases as the energy spectrum becomes harder; both the QPO frequency and amplitude are correlated with the PDS break frequency (f_{b2}); and finally there is an extra time delay (of hard X-rays) at the QPO frequency. Therefore, the QPO is likely associated with some resonant oscillation in the corona. If the hot electron corona is simply a post-shock region, it would not be hard to imagine the presence of shock-induced oscillations.

The observed PDS during the transition is very similar to that of some soft X-ray transients, such as GX 339–4 and GS 1124–68, often observed in a so-called “very high state” (VHS; Miyamoto et al. 1991; Ebisawa et al. 1994; Belloni et al. 1997). The VHS is characterized by the presence of QPO in the frequency range similar to ours here. Often, both the low-frequency red noise and white noise are present. Moreover, the QPO is thought to be associated with the oscillations in the corona that are triggered by a radiation pressure feedback loop, assuming the X-ray luminosity is super-Eddington in this state (van der Klis 1995). However, the QPO of Cyg X-1 during the transition cannot be due to radiation pressure because the X-ray luminosity is only a few percent of the Eddington luminosity. Recently, Belloni et al. (1997) showed that a QPO at 6.7 Hz was present in GS 1124–68 during the transition from its high state to low state. This bears remarkable similarity to what we see in Cyg X-1.

4. Conclusion

Based on our results, we conclude that both the white noise and low-frequency 1/f noise are intrinsic to soft “seed” photons. These intrinsic temporal properties are modified by the corona through Compton scattering process. Therefore, the change in the high-frequency characteristics (e.g., f_{b2}) is interpreted as evidence for a “fluctuating” corona during the spectral transitions. This scenario is supported by the measurement of hard X-ray time lags and coherence functions during the transition and in the soft state. The time lag scales roughly logarithmically with emerging photon energy, as predicted by thermal Comptonization models, thus is likely to be produced by such a process in the corona. This scaling relationship does not hold for the soft state, suggesting that new processes might be involved in the X-ray production.

The QPO persists during both the hard-to-soft and soft-to-hard transitions, but moves around between observations. For Cyg X-1, it is likely a coronal phenomenon because its centroid frequency and strength appear to be correlated with the hard X-ray properties, such as the energy spectrum, the PDS break frequency, and an extra time delay, that are tied to the corona. The presence of the QPO makes the PDS during the transition very similar to those of soft X-ray transients in the VHS.

Our results are consistent with many of the qualitative features predicted by the ADAF

model. Recently, the results from the study of long-term spectral evolution of Cyg X-1, based on the ASM and BATSE data, provide further evidence for the motion of the inner edge of the thin disk during the spectral transitions (Zhang et al. 1997), which is an important prediction of the model. However, the current version of the model still requires extreme values of α parameter to account for the observed X-ray luminosity of Cyg X-1 (Narayan 1996a). On the other hand, the bulk motion of relativistic electrons may indeed play a vital role in the soft state. The hard X-ray emission would then be produced by Comptonization due to the bulk motion of the electrons. Much can be learned by quantitatively applying these models to the spectral and temporal results from RXTE.

We wish to thank W. Zhang for the dead-time correction code, X. Hua and L. Titarchuk for many useful discussions. This work is supported in part by NASA Contract NAS5-30612.

Table 1. *RXTE* Observations of Cyg X-1

Obs.	Obs. Time (UT)	PCA Live Time (s)
1	5/22/96 17:44:00–19:48:00	4208
2	5/23/96 14:13:00–18:07:00	7936
3	5/30/96 07:46:00–08:44:00	2384
4	6/04/96 20:21:00–21:42:00	3280
5	6/16/96 00:00:00–00:40:00	816
6	6/16/96 04:45:00–05:43:00	1312
7	6/17/96 01:34:00–02:23:00	688
8	6/17/96 04:46:00–05:43:00	1312
9	6/17/96 07:58:00–09:07:00	2128
10	6/18/96 03:11:00–04:03:00	880
11	6/18/96 06:24:00–07:25:00	1680
12	6/18/96 09:36:00–10:45:00	2464
13	8/11/96 07:01:00–08:24:00	2688
14	8/11/96 15:08:00–15:51:00	1584
15	8/12/96 14:40:00–15:58:00	2114

Table 2. Characteristics of PDS during the Transitions

Obs.	Continuum					QPO				χ_ν/dof
	α_1	f_{b1} (Hz)	α_2	f_{b2} (Hz)	rms_c (%)	f_{qpo} (Hz)	FWHM (Hz)	rms_{qpo} (%)		
1a	$0.48_{-0.07}^{+0.09}$	$0.37_{-0.08}^{+0.02}$	$2.13_{-0.06}^{+0.08}$	$2.67_{-0.04}^{+0.05}$	$15.9_{-0.2}^{+0.2}$	$8.2_{-0.5}^{+0.4}$	$7.8_{-0.9}^{+0.9}$	$7.2_{-0.7}^{+0.6}$	1.1/103	
1b	$0.64_{-0.10}^{+0.07}$	$0.28_{-0.02}^{+0.04}$	$2.05_{-0.07}^{+0.12}$	$2.66_{-0.10}^{+0.05}$	$14.3_{-0.3}^{+0.2}$	$8.8_{-0.3}^{+0.2}$	$6.8_{-1.1}^{+1.4}$	$5.9_{-0.6}^{+0.9}$	1.2/103	
1c	$0.58_{-0.04}^{+0.04}$	$0.53_{-0.04}^{+0.05}$	$2.22_{-0.04}^{+0.06}$	$2.98_{-0.03}^{+0.03}$	$20.2_{-0.2}^{+0.2}$	$8.9_{-0.3}^{+0.2}$	$7.8_{-0.6}^{+0.7}$	$7.7_{-0.5}^{+0.6}$	1.1/103	
2a	$0.28_{-0.07}^{+0.08}$	$0.23_{-0.05}^{+0.04}$	$1.93_{-0.06}^{+0.19}$	$0.96_{-0.02}^{+0.09}$	$16.4_{-0.4}^{+0.3}$	$3.6_{-0.2}^{+0.3}$	$6.9_{-0.2}^{+0.3}$	$16.9_{-0.6}^{+0.6}$	1.6/103	
2b	$0.36_{-0.06}^{+0.05}$	$0.39_{-0.05}^{+0.11}$	$2.14_{-0.08}^{+0.10}$	$1.25_{-0.02}^{+0.03}$	$16.5_{-0.3}^{+0.4}$	$4.0_{-0.2}^{+0.2}$	$7.2_{-0.2}^{+0.1}$	$15.9_{-0.6}^{+0.5}$	1.8/103	
2c	$0.49_{-0.12}^{+0.18}$	$0.11_{-0.03}^{+0.03}$	$2.08_{-0.07}^{+0.08}$	$1.07_{-0.02}^{+0.03}$	$17.1_{-0.3}^{+0.4}$	$3.8_{-0.2}^{+0.2}$	$7.1_{-0.2}^{+0.1}$	$16.0_{-0.6}^{+0.5}$	1.2/103	
3	$0.68_{-0.08}^{+0.07}$	$0.32_{-0.03}^{+0.09}$	$1.97_{-0.04}^{+0.05}$	$2.81_{-0.03}^{+0.03}$	$15.0_{-0.2}^{+0.1}$	$9.4_{-0.2}^{+0.2}$	$6.6_{-0.8}^{+0.8}$	$5.8_{-0.4}^{+0.4}$	2.1/103	
13	$0.51_{-0.04}^{+0.07}$	$0.64_{-0.11}^{+0.06}$	$2.3_{-0.1}^{+0.1}$	$2.20_{-0.04}^{+0.03}$	$15.6_{-0.4}^{+0.4}$	$5.1_{-0.2}^{+0.3}$	$9.1_{-0.2}^{+0.2}$	$13.2_{-0.7}^{+0.7}$	1.8/103	
14	$0.78_{-0.04}^{+0.04}$	$0.79_{-0.04}^{+0.06}$	$2.09_{-0.03}^{+0.04}$	$3.45_{-0.04}^{+0.10}$	$18.0_{-0.1}^{+0.1}$	$12.3_{-0.8}^{+0.6}$	7_{-2}^{+2}	$3.0_{-0.5}^{+0.7}$	1.0/103	
15	$0.64_{-0.05}^{+0.04}$	$0.70_{-0.04}^{+0.08}$	$2.3_{-0.2}^{+0.2}$	$3.45_{-0.05}^{+0.05}$	$14.2_{-0.3}^{+0.3}$	$9.1_{-0.9}^{+0.9}$	14_{-2}^{+1}	7_{-1}^{+1}	1.2/103	

Table 3. Characteristics of PDS in the Soft State

Obs.	Continuum				QPO				χ_ν/dof
	α_1	α_2	f_b (Hz)	rms_c (%)	f_{qpo} (Hz)	FWHM (Hz)	rms_{qpo} (%)	χ_ν/dof	
4	$0.88^{+0.01}_{-0.01}$	$2.35^{+0.06}_{-0.06}$	$13.3^{+0.4}_{-0.4}$	$18.4^{+0.1}_{-0.2}$	$6.2^{+0.3}_{-0.3}$	5^{+1}_{-1}	$4.8^{+0.7}_{-0.6}$	1.1/104	
5	$1.01^{+0.04}_{-0.04}$	$2.4^{+0.4}_{-0.2}$	$13.5^{+0.7}_{-0.8}$	$18.6^{+0.4}_{-0.5}$	3^{+2}_{-3}	13^{+3}_{-3}	9^{+3}_{-3}	0.7/104	
6	$1.01^{+0.02}_{-0.01}$	$2.4^{+0.1}_{-0.1}$	$14.0^{+0.7}_{-0.5}$	$18.7^{+0.2}_{-0.2}$	$6.5^{+0.7}_{-0.7}$	6^{+2}_{-2}	4^{+1}_{-1}	1.4/104	
7	$0.95^{+0.01}_{-0.01}$	$2.6^{+0.2}_{-0.1}$	$12.8^{+0.6}_{-0.5}$	$16.6^{+0.2}_{-0.2}$	1.3/107	
8	$0.93^{+0.01}_{-0.01}$	$2.14^{+0.08}_{-0.06}$	$11.8^{+0.6}_{-0.4}$	$20.2^{+0.2}_{-0.2}$	$6.6^{+0.5}_{-0.3}$	$1.2^{+0.8}_{-0.7}$	$1.8^{+0.4}_{-0.4}$	1.2/104	
9	$1.01^{+0.01}_{-0.01}$	$1.88^{+0.02}_{-0.02}$	$6.4^{+0.2}_{-0.3}$	$23.2^{+0.2}_{-0.2}$	3.0/107	
10	$0.97^{+0.03}_{-0.03}$	$2.3^{+0.2}_{-0.1}$	$12.8^{+0.6}_{-0.8}$	$17.2^{+0.2}_{-0.3}$	$7.7^{+0.7}_{-0.9}$	10^{+3}_{-2}	6^{+2}_{-1}	0.9/104	
11	$0.99^{+0.01}_{-0.01}$	$2.6^{+0.1}_{-0.1}$	$13.6^{+0.5}_{-0.4}$	$17.5^{+0.2}_{-0.2}$	$6.5^{+0.4}_{-0.4}$	$1.6^{+1.5}_{-0.9}$	$1.6^{+0.5}_{-0.4}$	1.0/104	
12	$0.98^{+0.01}_{-0.01}$	$1.94^{+0.04}_{-0.03}$	$8.8^{+0.3}_{-0.2}$	$22.1^{+0.2}_{-0.2}$	1.5/107	

REFERENCES

Belloni, T. & Hasinger, G. 1990, A&A, 227, L33

Belloni, T., Méndez, M., van der Klis, M., Hasinger, G., Lewin, W. H. G., & van Paradijs, J. 1996, ApJ, 472, L107

Belloni, T., van der Klis, M., Lewin, W. H. G., van Paradijs, J., Dotani, T., Mitsuda, K., & Miyamoto, S. 1997, A&A, in press

Bendat, J., & Piersol, A. 1986, “Random Data; Analysis and Measurement Procedures” (New York: Wiley & Sons)

Bolton, C. T. 1972, Nature, 235, 271

Bowyer, S., Byram, E. T., Chubb, T. A. & Friedman, H. 1965, Science, 147, 394

Bradt, H. V., Rothschild, R. E., & Swank, J. H. 1993, A&AS, 97, 355

Chakrabarti, S. K., & Titarchuk, L. 1995, ApJ, 455, 623

Cui, W. 1996, IAU Circ. 6404

Cui, W., Focke, W., & Swank, J. 1996, IAU Circ. 6439

Cui, W., Heindl, W. A., Rothschild, R. E., Zhang, S. N., Jahoda, K., & Focke, W. 1997a, ApJ, 474, L57

Cui, W., Zhang, S. N., Heindl, W. A., Rothschild, R. E., Jahoda, K., Focke, W., & Swank, J. H. 1997b, Proceedings of 2nd Integral workshop “The Transparent Universe”, Eds: C. Winkler et al. (St. Malo, France), ESA-SP 382, in press (astro-ph/9610072)

Dolan, J. F., Crannell, C. J., Dennis, B. R., Frost, K. J., & Orwig, L. E. 1977, Nature, 267, 813

Ebisawa, K., et al. 1994, PASJ, 46, 375

Ebisawa, K., Titarchuk, L., & Chakrabarti, S. K. 1996, PASJ, 48, 59

Gierliński, M, et al. 1996, MNRAS, in press

Gies, D. R., & Bolton, C. T. 1982, ApJ, 260, 240

Gies, D. R., & Bolton, C. T. 1986, ApJ, 304, 371

Holt, S. S., Boldt, E. A., Serlemitsos, P. J., & Kaluziensky, L. J. 1979, ApJ, 203, L63

Hua, X., & Titarchuk, L. 1996, ApJ, 496, 280

Jahoda, K., et al. 1996, EUV, X-ray, and Gamma-ray Instrumentation for Astronomy VII, O. H. W. Siegmund and M. A. Gummin, eds., SPIE 2808, p. 59

Kazanas, D., Hua, X., Titarchuk, L. 1996, ApJ, in press

Levine, A., et al. 1996, ApJ, 469, L33

Ling, J. C., Mahoney, W. A., Wheaton, W. A., & Jacobson, A. S. 1987, ApJ, 321, L117

Miyamoto, S., Kitamoto, S., Mitsuda, K., & Dotani, T. 1988, Nature, 336, 450

Miyamoto, S., Kimura, K., Kitamoto, S., Dotani, T., & Ebisawa, K. 1988, ApJ, 383, 784

Morgan, E. H., Bradt, H., Levine, A. M., & Remillard, R. 1994, EDS Observer's Manual

Narayan, R., & Yi, I. 1994, ApJ, 428, L13

Narayan, R. 1996a, ApJ, 462, 136

Narayan, R. 1996b, Proc. IAU Colloq. 163 on "Accretion Phenomena & Related Outflows", A.S.P. Conf. Series, eds. D. T. Wickramasinghe, L. Ferrario, G. V. Bicknell, in press

Payne, D. G. 1980, ApJ, 441, 770

Phlips, B. F., et al. 1996, ApJ, 465, 907

Phlips, B. F., et al. 1996, ApJ, in preparation

Shapiro, S. L., Lightman, A. P., & Earley, D. M. 1976, ApJ, 204, 187

Shakura, N. I., & Sunyaev, R. A. 1973, A&A, 24, 337

Sunyaev, R. A., & Titarchuk, L. G. 1980, A&A, 86, 121

Tanaka, Y., & Lewin, W. H. G. 1995, in "X-ray Binaries", eds. W. H. G. Lewin, J. van Paradijs, & E. P. J. van den Heuvel (Cambridge U. Press, Cambridge) p. 126

Titarchuk, L., Mastichiadis, A., & Kylafis, N. D. 1996, A&A, in press

Titarchuk, L. 1997, Proceedings of 2nd Integral workshop "The Transparent Universe", Eds: C. Winkler et al. (St. Malo, France), ESA-SP 382, in press

van der Klis, M. 1995, in "X-ray Binaries", eds. W. H. G. Lewin, J. van Paradijs, & E. P. J. van den Heuvel (Cambridge U. Press, Cambridge) p. 252

Vaughan, B., & Nowak, M. 1997, ApJ, 474, L43

Webster, B. L., & Murdin, P. 1972, Nature, 235, 37

Zhang, S. N., Harmon, B. A., & Paciesas, W. S., 1996, IAU Circ. 6447

Zhang, S. N., Cui, W., Harmon, B. A., Paciesas, W. S., Remillard, R. E., & van Paradijs, J. 1997, ApJ, in press (astro-ph/9701027)

Zhang, W., Jahoda, J., Swank, J. H., Morgan, E. H., & Giles, A. B. 1995, *ApJ*, 449 930

Zhang, W., Morgan, E. H., Jahoda, K., Swank, J. H., Strohmeyer, T. E., Jernigan, G., & Klein, R. I. 1996, *ApJ*, 469, L29

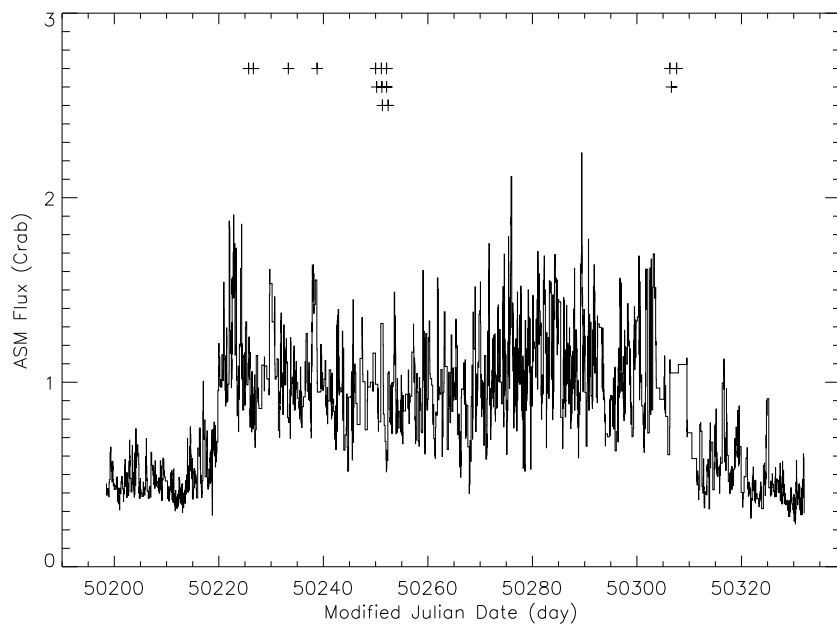


Fig. 1.— ASM light curve of Cyg X-1. It comprises measurements from individual “dwells” with 90-second exposure time. The crosses indicate when the *RXTE* observations were made. MJD 50213.0 corresponds to 1996 May 10 0 h UT.

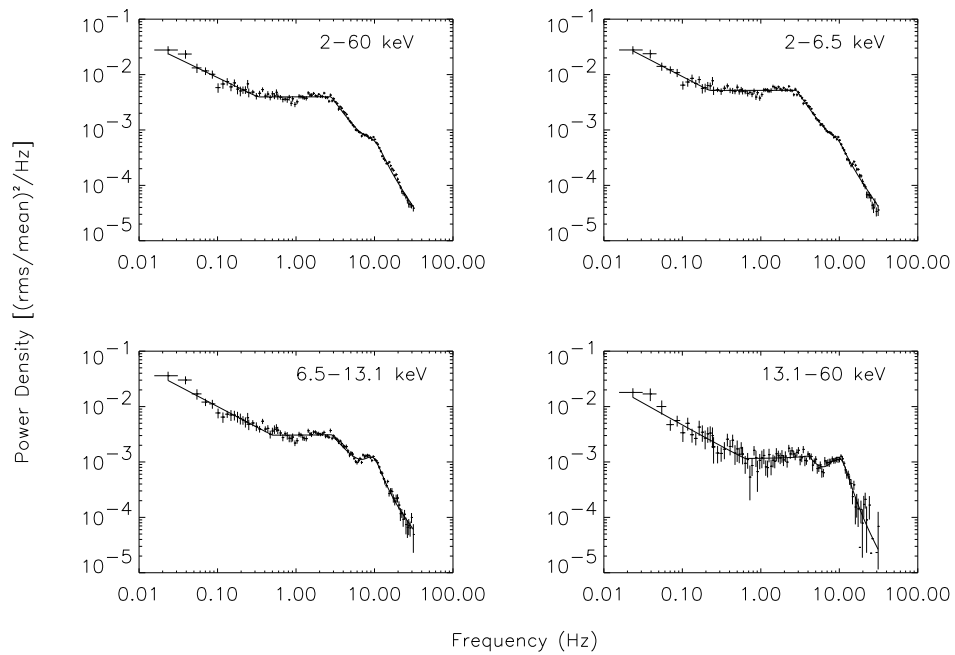


Fig. 2.— Power density spectrum of Observation #3 (see Table 1) in the energy bands indicated. It is a representative of the hard-to-soft transition. The data are logarithmically rebinned to reduce scatter at high frequencies. The solid line shows the best-fit model.

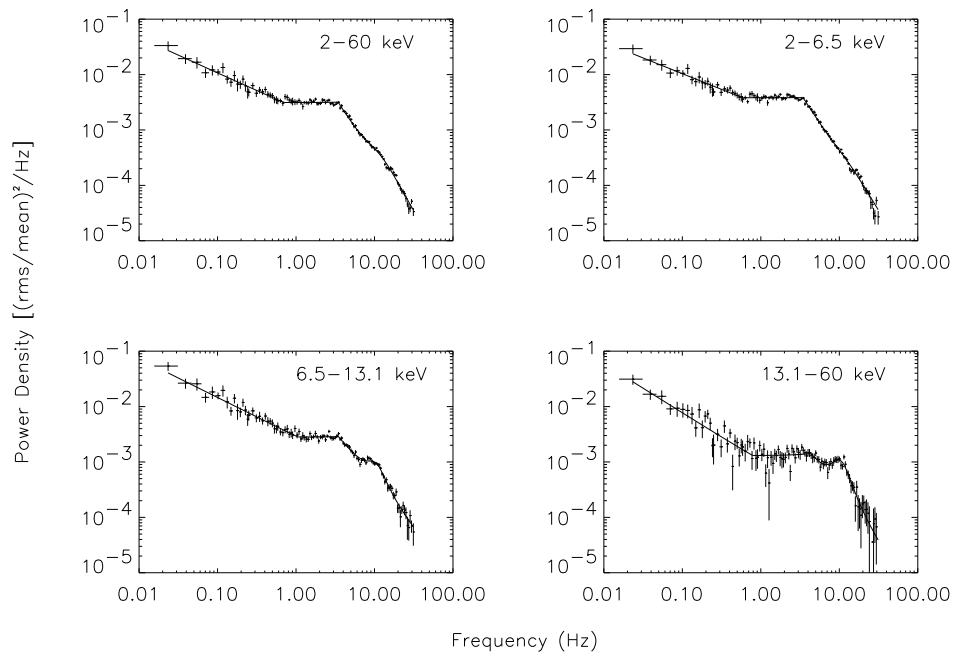


Fig. 3.— Power density spectrum of Observation #15 (see Table 1) in the energy bands indicated. It is a representative of the soft-to-hard transition. The data are logarithmically rebinned to reduce scatter at high frequencies. The solid line shows the best-fit model.

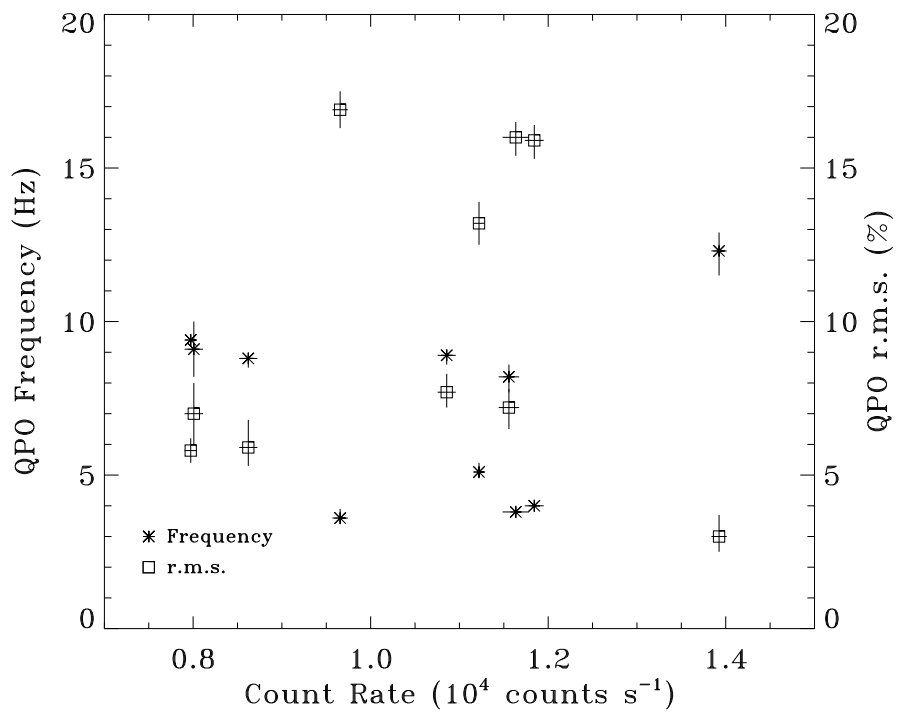


Fig. 4.— QPO characteristics at various source count rates. No apparent correlation can be seen.

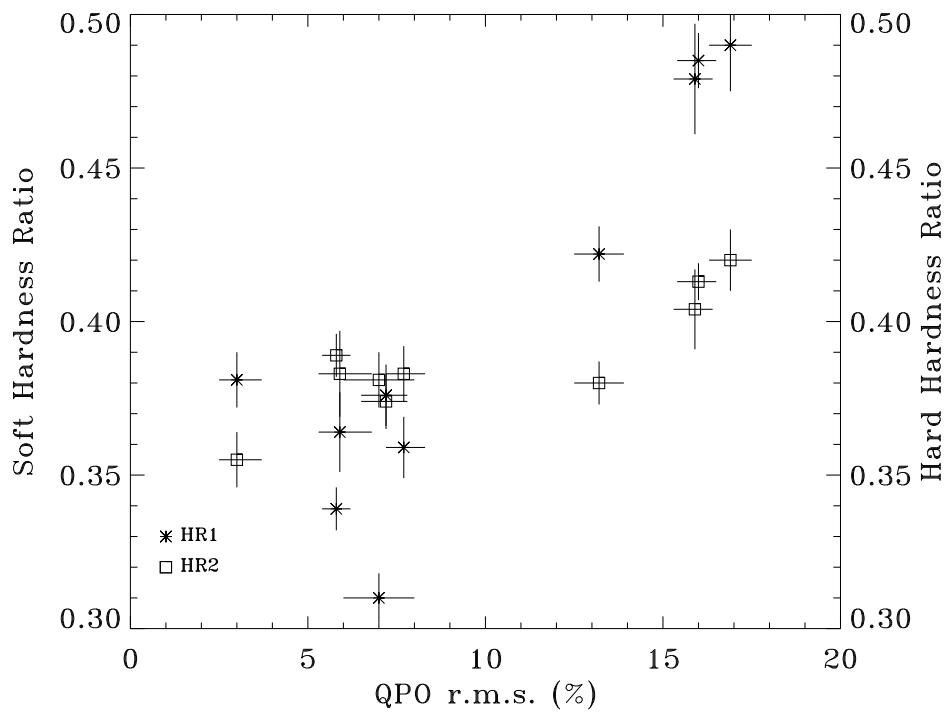


Fig. 5.— Spectral dependence of the QPO amplitude. HR1 and HR2 are defined in Section 2.1.1.

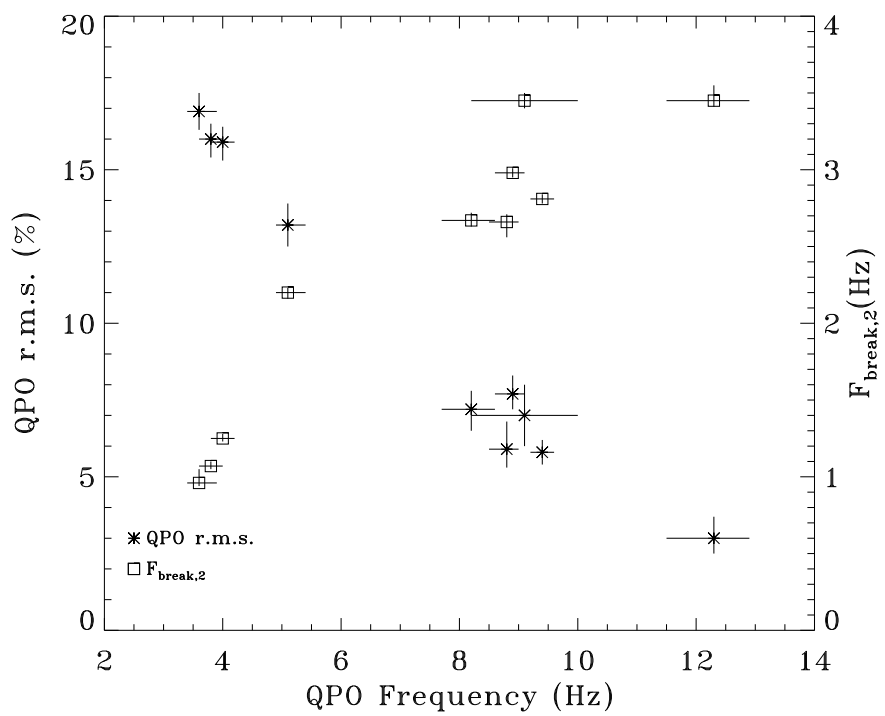


Fig. 6.— QPO frequency, QPO amplitude, the PDS break frequency, and correlations between them.

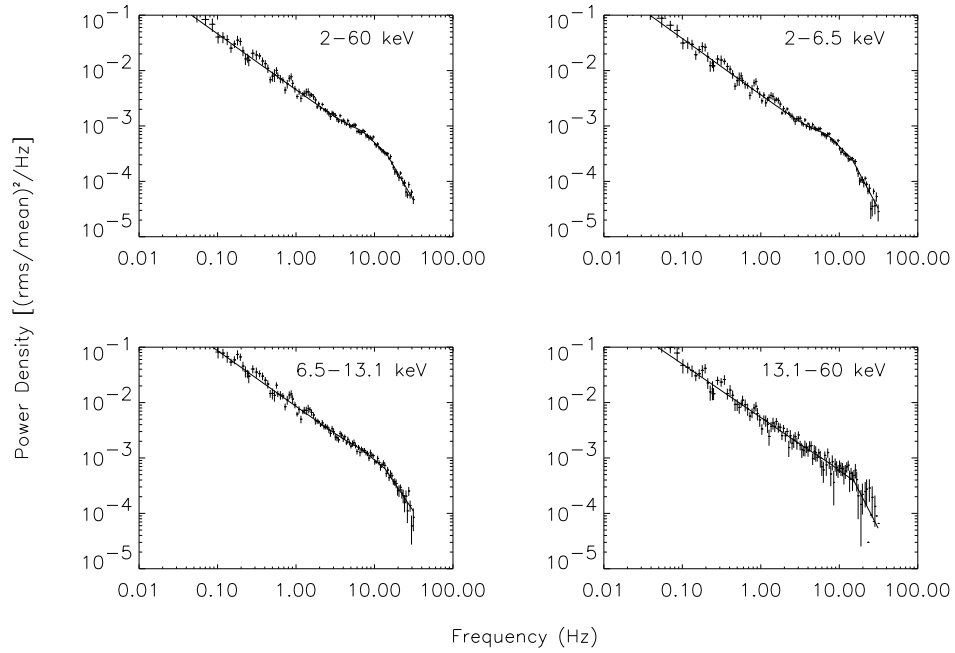


Fig. 7.— Power density spectrum of Observation #6 (see Table 1) in the energy bands indicated. It is a representative of the soft state. The data are logarithmically rebinned to reduce scatter at high frequencies. The solid line shows the best-fit model.

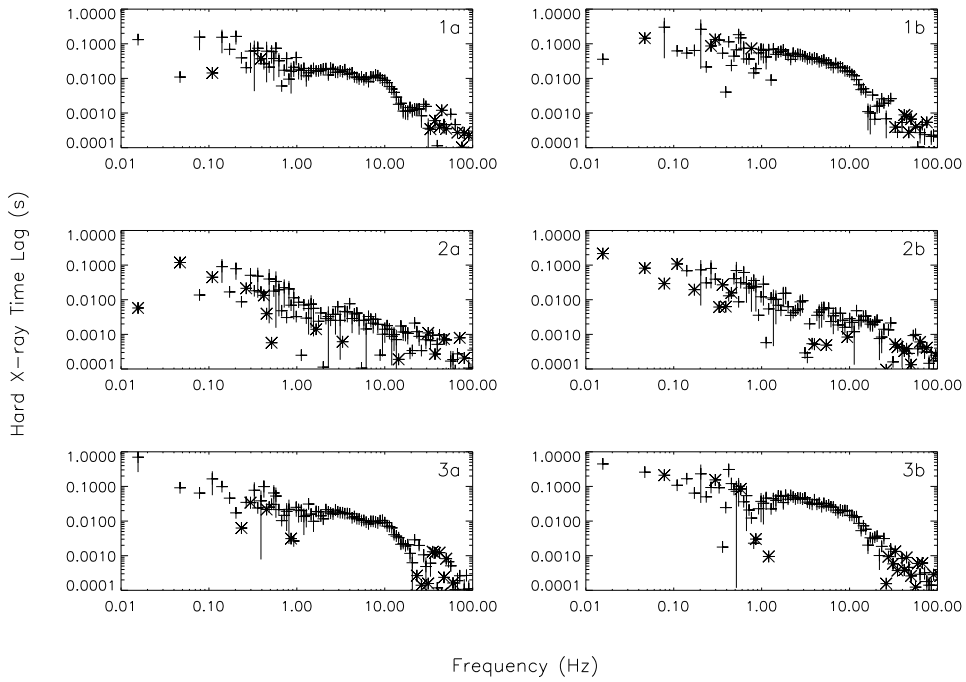


Fig. 8.— Hard X-ray time lag. Three panels on the left (top to bottom) show in crosses the measurements between the soft and medium bands for Observations #3, #6, and #15, respectively, and the right panels between the soft and hard bands. The error bars that extend to negative values are not plotted. The asterisks indicate negative values.

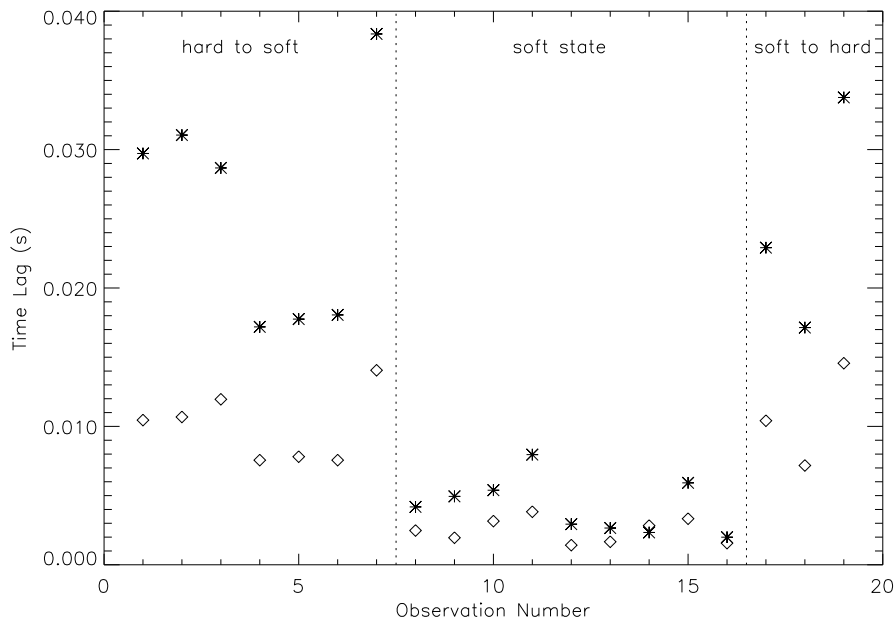


Fig. 9.— “Effective” time lags for all observations (see definition in Section 2.2.1). The diamonds show the measurements between the soft and medium bands, and the asterisks between the soft and hard bands. Three distinct phases during the entire period are marked, and separated by dotted-lines.

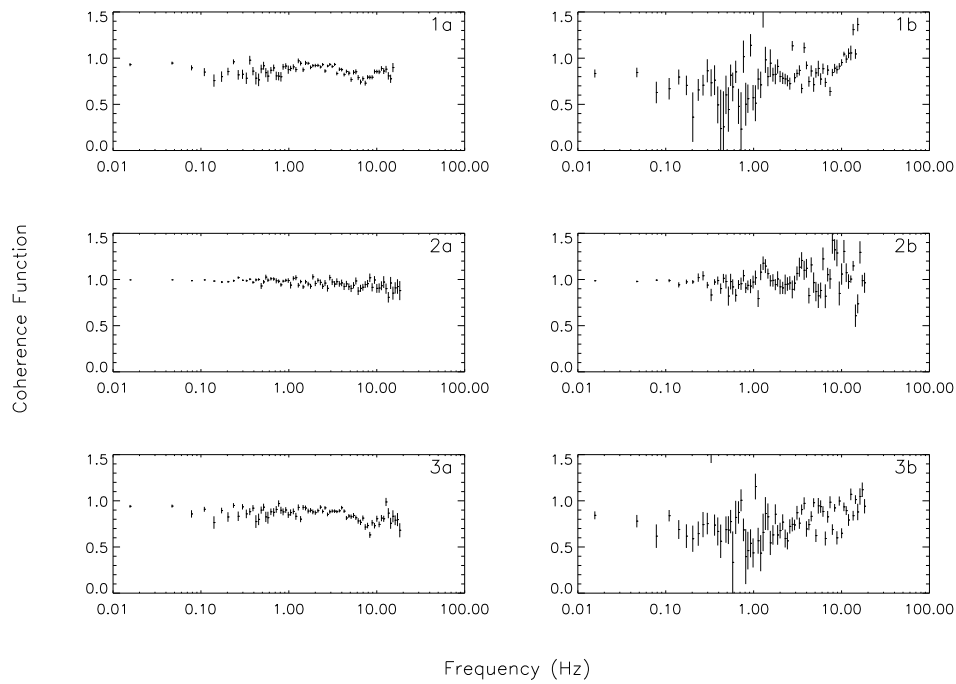


Fig. 10.— Coherence function. Three panels on the left (top to bottom) show the measurements between the soft and medium bands for Observations #3, #6, and #15, respectively, and the right panels between the soft and hard bands.

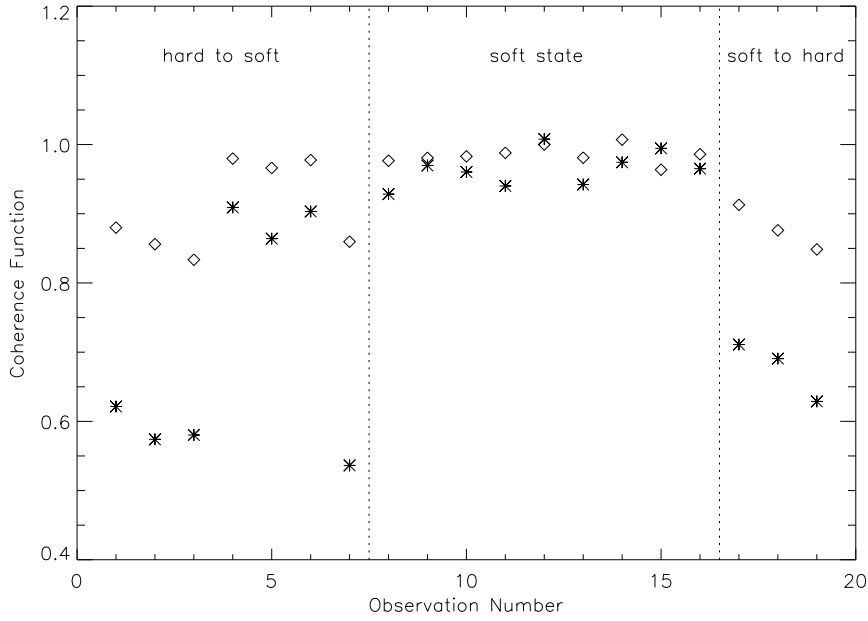


Fig. 11.— Average coherence function for all observations (see text). The diamonds show the measurements between the soft and medium bands, and the asterisks between the soft and hard bands. Three distinct phases during the entire period are marked, and separated by dotted-lines.